

Research on the temperature control strategy of thin-wall parts fabricated by laser direct metal deposition

Tianbiao Yu (✉ tianbiaoyudx@gmail.com)

Northeastern University <https://orcid.org/0000-0002-6161-8838>

Liaoyuan Chen

Zhe Liu

Pengfei Xu

Research Article

Keywords: Laser direct metal deposition, Thin-walled part, Finite element model, Heat accumulation, Optimized strategy, Mechanical properties

Posted Date: July 12th, 2022

DOI: <https://doi.org/10.21203/rs.3.rs-1010799/v1>

License:  This work is licensed under a Creative Commons Attribution 4.0 International License.

[Read Full License](#)

Research on the temperature control strategy of thin-wall parts fabricated by laser direct metal deposition

Tianbiao Yu*, Liaoyuan Chen, Zhe Liu, Pengfei Xu

School of Mechanical Engineering and Automation, Northeastern University, Shenyang,
China.

Current author list:

Name: Tianbiao Yu	E-mail: tianbiaoyudyx@gmail.com
Name: Liaoyuan Chen	E-mail: chen1910113@163.com
Name: Zhe Liu	E-mail: zheliu321@163.com
Name: Pengfei Xu	E-mail: xupengfei@me.neu.edu.cn

Abstract

To solve the problem that the macro-size, microhardness, and mechanical properties of the laser direct metal deposition (DMD) of thin-walled parts are inconsistent due to the heat accumulation, an improved three-dimensional finite element heat propagation model was developed to simulate the temperature evolution of the single-pass multi-layer thin-walled parts. The results show that the heat accumulation is contributed to the transformation of the heat dissipation mechanism from three-dimensional to two-dimensional, while the residual heat of the former layer has no significant effect on the heat accumulation of the current layer. The optimized strategy of decreasing laser power gradually is more effective than the optimized strategy of increasing the time interval between layers in maintaining the stability of the molten pool. The integrated optimized strategy of parabolic-shape laser power decreasing and time interval of 5 s is the most effective method to reduce the heat accumulation in the DMD of thin-walled parts. The thin-walled parts with an optimized deposition process have a more uniform width, finer microstructure, and higher microhardness. This work provides theoretical guidance for reducing the heat accumulation during DMD thin-walled parts and is beneficial to improving the uniformity of mechanical properties of thin-walled parts.

Keywords: Laser direct metal deposition; Thin-walled part; Finite element model; Heat accumulation; Optimized strategy; Mechanical properties

1. Introduction

Laser direct metal deposition (DMD), as one of the advanced additive manufacturing (AM) technology, has been widely used in the manufacture of parts with complex and thin-walled structures due to its design flexibility, dieless manufacturing, and rapid response to market demand and other advantages [1,2,3]. Since the DMD has the characteristics of rapid melting and cooling, the thermal behavior during the deposition process has a significant impact on the microstructure and mechanical properties after solidification [4,5]. Especially in the process of DMD of thin-walled parts, it is of great interest to analyze the thermal histories for manufacturing parts with desired microstructure and mechanical properties.

In the process of DMD of thin-walled parts, with the gradual increase of deposition layers, the heat dissipation mode of the molten pool would gradually change from three-dimensional to two-dimensional [6,7]. This phenomenon would worsen the heat dissipation of the molten pool, and then affect macro-morphology by the shape of stable molten pool and microstructure by solidification parameters (temperature gradient and solidification rate), and finally results in the uniformity of mechanical properties of thin-walled parts. To solve the problem of instability of thermal behavior in DMD of thin-walled parts, some researches on molten pool monitoring and numerical simulation have been carried out. In the process of fabricating 316LSi thin-walled parts with a robotized laser/wire direct metal deposition system, Akbari et al. [8] monitored the molten pool in real-time with a CMOS camera and obtained an empirical correlation between the molten pool area and the cooling rate. This study also found that the molten pool area gradually increases with the increase of the number of layers of thin-walled parts. To ensure the stability of the molten pool size in the process of DMD of thin-walled parts, Zhu et al. [7] used an infrared thermal imager to record the maximum temperature of the molten pool. According to the measurement results, a control strategy of reducing power layer by layer was proposed to eliminate the change in pool size caused by energy accumulation. Besides, numerical simulation is also another effective method to reveal the thermal history of thin-walled parts during the DMD process. Xiong et al. [9] established a finite element model of heat conduction for the manufacturing of the circular thin-walled part using gas metal arc welding technology. The results indicate that the temperature gradient of the molten pool decreases with the increase of deposition height and the main direction of heat conduction changes from axial to circumferential. In the coupled finite element model of temperature field

and flow field of thin-walled parts established by Simon et al. [10], the effects of process parameters on the width and length of the molten pool and the surface finish of the solidified part are discussed in detail. The results also point out that the molten pool size increases from the first layer to the fifth layer, which is attributed to the energy storage in the continuous deposition process. Xia et al. [11] characterized the complex thermal history of thin-walled metal parts fabricated by DMD through numerical simulation and experiments. From the results, the cumulative effect of heat increases the peak temperature of the molten pool, while the decreasing cooling rate reduces nucleation rate at the beginning of solidification, which coarsens austenite grains at the top of the part.

Reviewing the above kinds of literature, it is very important to optimize the thermal behavior of the molten pool during the DMD process for the microstructure and mechanical properties of the parts. The methods to reduce the heat accumulation during the DMD process mainly include improving the heat dissipation ability of the molten pool and controlling the energy input [12,13,14]. For the former method, the parts need to be forced cooled [15], which is difficult to carry out in terms of equipment and deposition process. At the same time, controlling the input of laser energy to slow down or suppress heat accumulation is a convenient and effective method. Besides, the previous researches focus on the temperature change in the building direction, but the temperature change in the scanning direction is often ignored. Therefore, in this study, the temperature evolution on both the building direction and scanning direction during the DMD of the thin-walled part was studied by an established finite element model. And then, different power control strategies and interlayer intervals were selected to ensure the stability of the molten pool during the DMD process. Finally, combined with the results of simulation and experiment, the effects of cooling rate, solidification rate at the solid-liquid interface, and thermal history on the microstructure and microhardness of thin-walled parts were analyzed in detail.

2 Experimental method

The equipment used in this study is an integrated DMD system, as shown in Fig. 1. The hardware parts of the equipment mainly include a robot arm (KR16-2 with six freedom degrees, KUKA Robotics Corporation), a continuous wave (CW) laser generator (YLP-500, IPG, Germany, the wavelength of 1020 nm), a cladding head with a coaxial powder nozzle (RC52), a water cooler (Tongfei cooling SL400), a controller, and an electric control cabinet. The

cladding head is mounted on the end effector of the robot arm, which ensures the flexible design and implementation of the deposition strategy. The deposition track is programmed, optimized, and simulated by offline programming software (Robot-Art), and then imported into the KUKA controller after post-processing. The program can sensitively control the scanning speed, track spacing, and laser on and off. The laser power and powder feed rate can be adjusted online manually during the DMD process. Argon with a purity of 99.99% is used as the shielding gas and carrier gas to reduce the oxidation of the deposited materials.

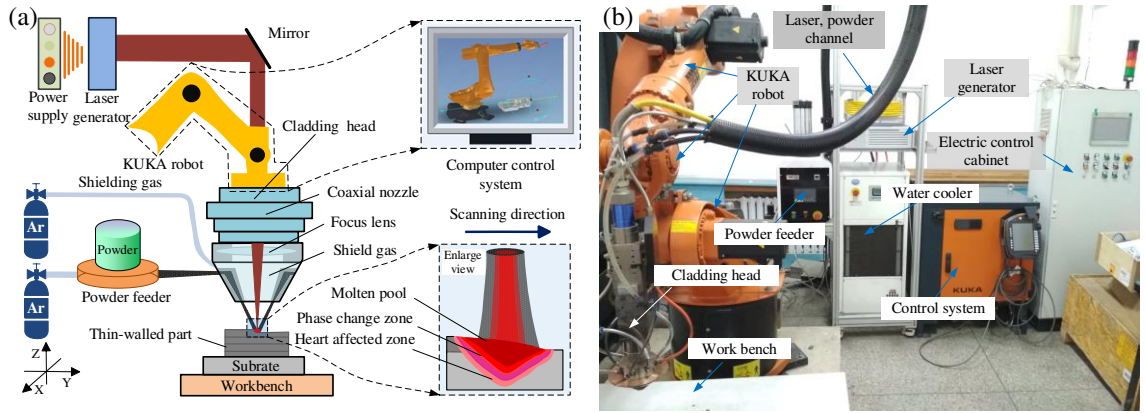


Fig. 1. The DMD system for experimental, (a) schematic illustration; (b) experimental setup.

The commercial medium carbon steel (45 steel) was selected as the substrate with a size of $100 \times 100 \times 10$ mm³. The Fe-based powders were used as the deposition material. The chemical composition of the deposition material and substrate is shown in Table 1. As shown in Fig. 2, the diameter of spherical particles are ranged from 42.31 μm to 184.67 μm , and more than 99.73% of the particles are around 71.46–140.47 μm . Before the experiment, the surface of the substrate was ground with 800# sand paper and cleaned with alcohol to remove dirt. The powders were dried in a constant temperature drying oven at 80 °C for 3 hours. The process parameters for the experiment and simulation are shown in Table 2.

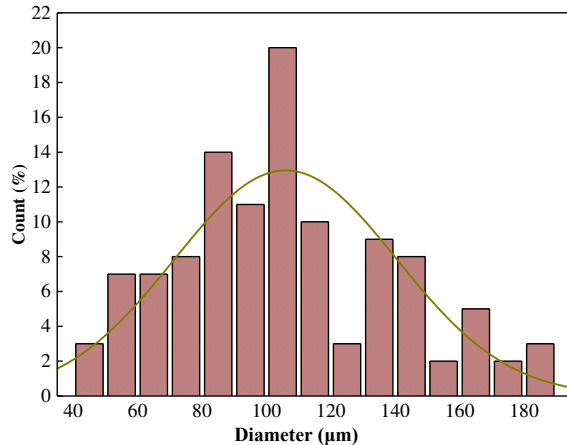


Fig. 2. The size distribution mapping of the Fe-based powders.

Table 1 Chemical compositions of 316L powder and standard 45 steel.

Element (wt.%)	C	Cr	B	Si	Ni	Mn	P	Fe
Fe-based powder	0.1-0.2	14-18	1.0-2.0	1.0-1.5	2.0-2.5	0.2-0.5	-	Bal.
45 steel	0.42-0.50	≤ 0.2	-	0.17-0.37	≤ 0.30	0.50-0.80	≤ 0.035	Bal.

Table 2 Deposition parameters for Fe-based powder.

Parameters	Values & units
Output power (P)	390 W
Powder feed rate (V_F)	174 mg/s
Scanning speed (V_s)	5.0 mm/s
Laser beam diameter (d)	1.0 mm
Z-axis increment (ΔZ)	0.29 mm
Number of layers (N)	20
Laser absorptivity	0.4

After the experiment, the samples for metallographic examination were cut from by thin-walled parts using the wire cut electrical discharge machining perpendicular to the scanning direction, and then they were ground by different types of sandpaper from 240# to 2000#, mechanically polished through the diamond paste and then corroded with a mixed solution of 50 mL hydrochloric acid (HCl), 25 mL water (H_2O) and 5 g $FeCl_3$. The cross-section morphology and microstructure were obtained by 3D laser microscopy (OLS4000, Japan). The micro-hardness of thin-walled parts was measured by a Vickers microhardness tester (HV-1000, Shanghai, China), with a load of 300gf and a load-dell time of 10s along the building direction.

3. Numerical simulation process

Since DMD is a complex physical and chemical process, this study focuses on optimizing the temperature control strategy by simulating the temperature accumulation of thin-walled parts during the deposition process, thus following assumptions and simplification are made to simplify the finite element model:

- (1) The deposition material is isotropic and homogeneous media;
- (2) The material vaporization is not considered during the modeling process;
- (3) Neglecting the influence of shielding gas and carrier gas on temperature distribution;
- (4) The effect of strain and stress field on temperature field is neglected.

3.1 Governing equations

The thermal behavior of the DMD process mainly includes: (a) heat conduction between layers, (b) thermal radiation, and convection between deposited parts and the atmosphere [16,17]. The classical nonlinear heat conduction equation can be expressed as Eq. (1) [18],

$$\rho c_p \frac{\partial T}{\partial t} = \frac{\partial}{\partial x} \left(k \frac{\partial T}{\partial x} \right) + \frac{\partial}{\partial y} \left(k \frac{\partial T}{\partial y} \right) + \frac{\partial}{\partial z} \left(k \frac{\partial T}{\partial z} \right) + Q_{\text{int}} \quad (1)$$

where k is the thermal conductivity (W/m/K), c_p is the specific heat capacity (J/Kg/K), Q_{int} is the input heat and T and t is the temperature (°C) and time (s), respectively.

In the boundary conditions, thermal conductivity normal to the surface, thermal radiation and convection, and boundary heat flux of laser beam can be described by Eq. (2) [19],

$$k(\nabla T \cdot n) + h_c(T - T_{\text{amb}}) + \varepsilon \cdot \sigma(T^4 - T_{\text{amb}}^4) + q(x, y, z, t) = 0 \quad (2)$$

where h_c is the convective heat transfer coefficient between the air and model (W/m²/K), T_{amb} is the ambient temperature (20 °C), ε is the emissivity, σ is the Stefan-Boltzmann constant (5.67×10^{-8} W/m²/K⁴), $q(x, y, z)$ represents the input heat flux of the laser beam. During the DMD, the moving laser beam with a double ellipsoidal heat distribution was employed when the penetration depth of laser to the material was considered, as shown in Fig. 3. The input heat flux can be defined as Eq. (3),

$$q(x, y, z, t) = \begin{cases} \frac{6\sqrt{3}f_f\eta P}{\pi^{3/2}a_1bc} \exp\left(\frac{-3x^2}{a_1^2} + \frac{-3y^2}{b^2} + \frac{-3z^2}{c^2}\right) & x > x_0 \\ \frac{6\sqrt{3}f_r\eta P}{\pi^{3/2}a_2bc} \exp\left(\frac{-3x^2}{a_2^2} + \frac{-3y^2}{b^2} + \frac{-3z^2}{c^2}\right) & x < x_0 \end{cases} \quad (3)$$

where P is the laser power (W), η is the laser absorptivity of the molten pool, f_f (1.4) and f_r (0.6) are factors of the heat flux in the front and rear halves, a_1 , a_2 , b , and c are characteristic parameters of the heat source model, as shown in Fig. 3.

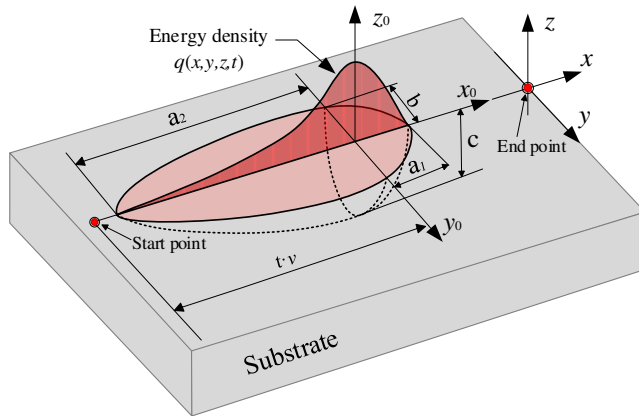


Fig. 3. Schematic diagram of the double ellipsoid heat source model.

3.2 Thermophysical properties

Previous numerical simulations [1,20,21] have shown that the thermophysical properties of the material have a significant influence on the results. The deposited materials undergo a

rapid melting and cooling process ($>10^6$ K/s) during the DMD process. Therefore, it is very significant to get more accurate simulation results to regard the physical properties of the deposited materials as changing with temperature. Since the physical parameters of Fe-based powder and substrate have not been calibrated, the thermodynamic calculation based on the widely accepted Calculation of Phase Diagrams (CALPHAD) method was used to evaluate the physical parameters of deposited materials [22,23,24]. The thermal physical properties of deposited materials are represented in Fig. 4.

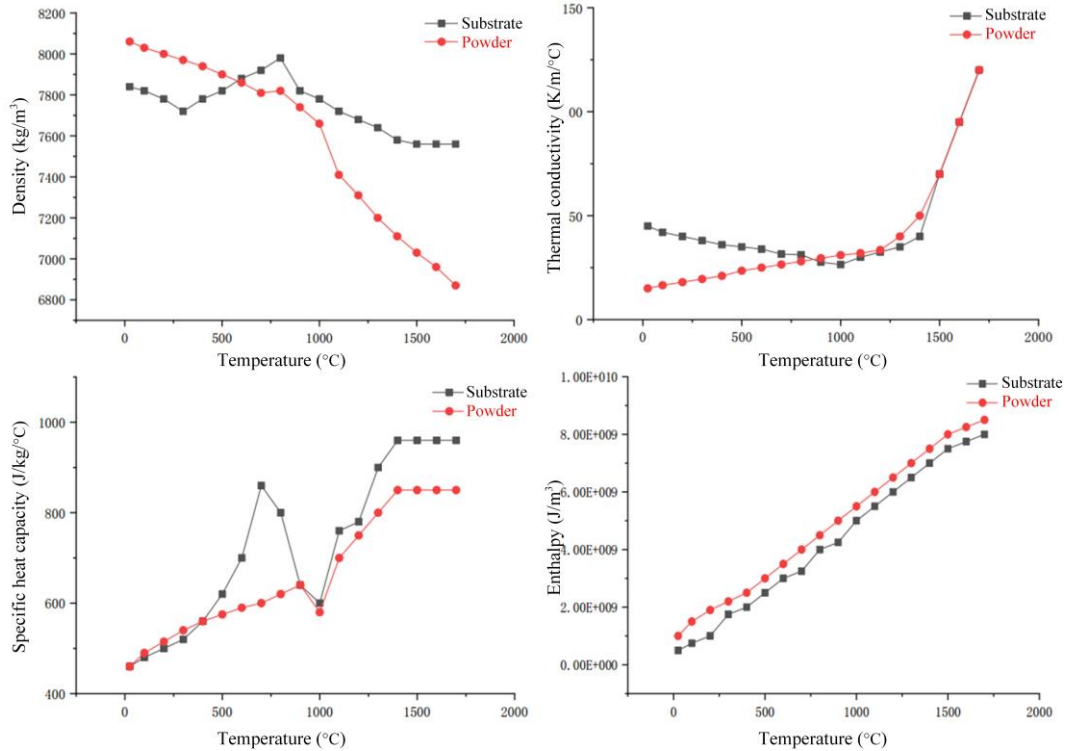


Fig. 4. Material properties of metal powder and substrate for the DMD model.

3.3 Finite element model set-up

Fig. 5 illustrates the geometrical model and meshing of a typical thin-walled part with 20-layers. The geometric model and the load are symmetrical, so half of the fully symmetric model was selected to improve the computational efficiency. The calculation domain mainly includes a substrate with the size of $40 \times 12 \times 5$ mm³ and the thin-walled part with the size of $30 \times 0.6 \times 5.8$ mm³. In this study, the arc was used to express the cross-section of the single-pass deposition track, which makes the computed results more consistent with the experimental than the commonly used rectangular section [25,26,27]. The deposition path of the thin-walled part is also shown in Fig. 5(a). In the process of simulation, the size of the meshing is often inversely proportional to the computational efficiency and accuracy [18]. The temperature distribution in the deposition

region is relatively concentrated, so the grid in this region is refined, and the grid in other regions is gradually coarse. The generated meshing is shown in Fig. 5(b).

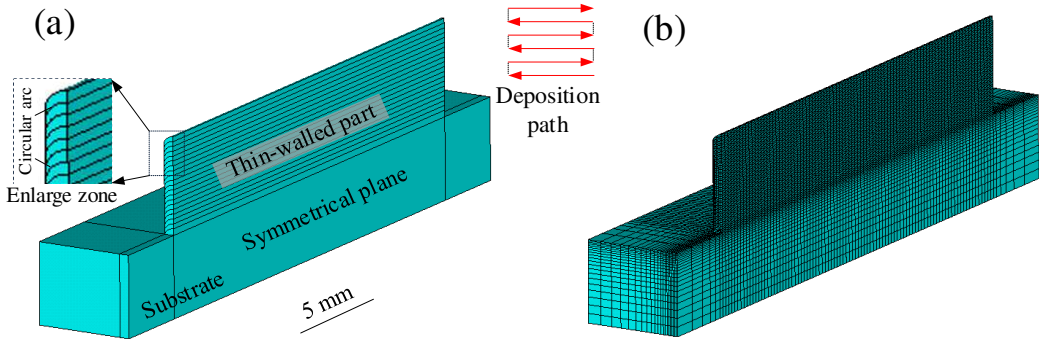


Fig. 5. (a) Geometrical model and (b) finite element meshing.

In the process of the DMD process, the generation and boundary conditions of the signal-pass deposited track are dynamic, so the "element birth and death technique technology" was used to simulate the spatiotemporal growth process of the deposition track [28]. As shown in Fig. 6, the elements in different positions are activated in turn according to the position of the laser beam. Cells within the laser beam range are active, while others are inactive and do not participate in the current calculation. At the same time, according to the building state of the deposited track, the boundary conditions are updated step by step to simulate the real DMD process. The details of setting and solving the finite element model are shown in Fig. 7.

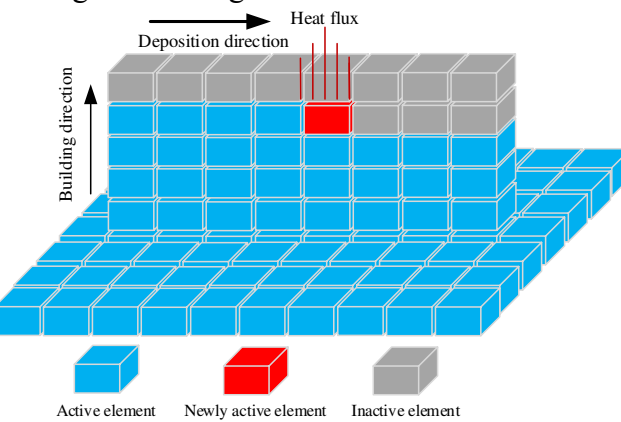


Fig. 6. Schematic diagram of element birth and death technique.

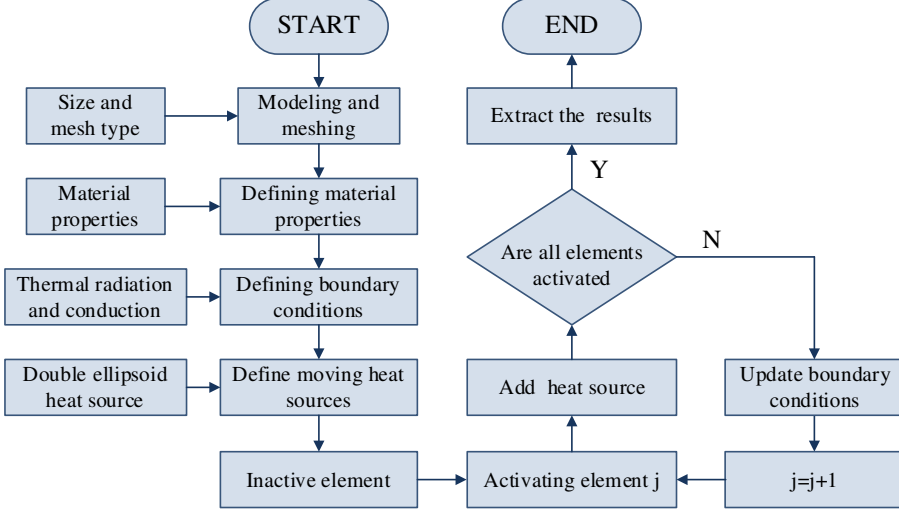


Fig. 7. The calculation process of simulating the DMD process.

4 Results and discussion

4.1 Temperature distribution

Fig. 8 shows the computed temperature distribution of the 20-layer thin-walled part when the heat source is respectively located at the middle points of the different layers. As the heat source moves, the finite element elements are activated gradually along the scanning direction. The temperature of the front of the comet-shaped molten pool is high, while the temperature of the rear is low. Besides, with the increase of the number of deposition layers, the maximum temperature of the molten pool becomes higher and higher. The maximum temperature of the molten pool in the 18th layer is 350 °C higher than that in the 3rd layer. As a result, the melt pool is becoming larger, which significantly increases the powder catchment efficiency and thus destroys the width uniformity. In the process of DMD, the heat dissipation of the molten pool can be divided into two types: (a) heat conduction by the previously deposited layer, (b) atmospheric convection and radiation [29]. The heat accumulation can be expressed as follow:

$$Q_{\text{cum}} = \int_0^t q(x, y, z, t) dt - \left(\int_0^t h_{\text{cond}} dt + \int_0^t h_{\text{conv}} dt + \int_0^t h_{\text{rad}} dt \right) \quad (4)$$

where Q_{cum} is the heat accumulation, $q(x, y, z)$ is input heat flux of the laser beam (Eq. 3), h_{cond} is the heat conduction to substrate or previously deposited layer, h_{conv} and h_{rad} are the convection and radiation to the atmosphere, respectively.

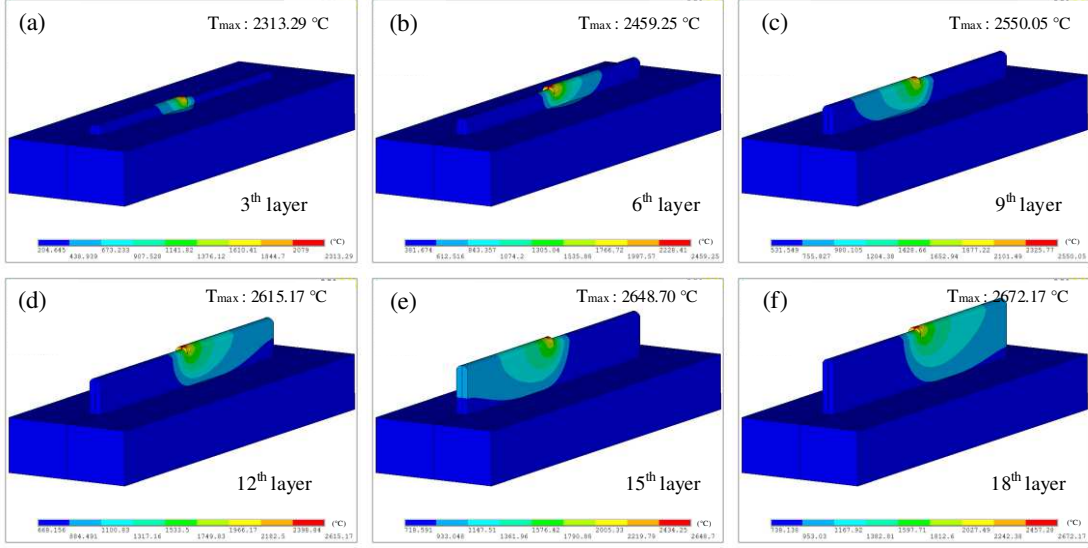


Fig. 8. Temperature distribution on different layers during the DMD process.

To analyze the heat accumulation characteristics of thin-walled parts fabricated by the DMD in detail, the temperature history of the nodes where the laser beam is located (shown in Fig. 8) is obtained, and the results are shown in Fig. 9. The temperature history of points from A₁ to A₆ has a similar trend, and there are some temperature peaks and troughs. It can be found from Fig. 9 that the temperature at the nodes rises very quickly, whereas it does fall very slowly. The compression of the metal liquid in the front of the molten pool led to the rapid temperature rise in the front of the molten pool [30]. The slow dissipation of heat in the tail of the molten pool leads to a slow drop in temperature. As the DMD process, the temperature of the nodes is significantly higher than that of the nodes of the former deposited layer, but the temperature change tends to be stable. Besides, the phenomenon that the temperature peak of each node is higher and higher is mainly due to the gradual heat accumulation.

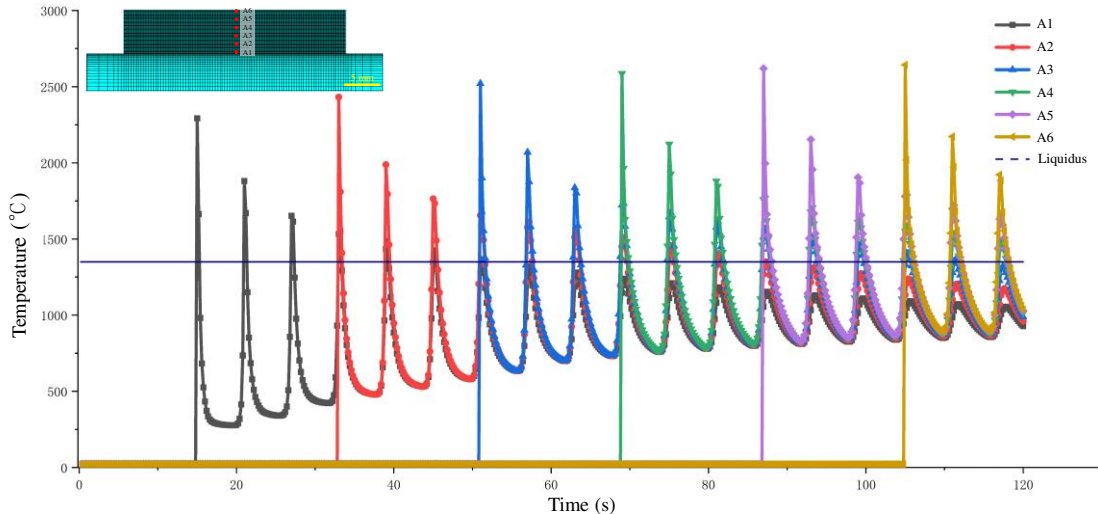


Fig. 9. Thermal cycle curves of the middle points in the different layers.

Since the heat dissipation of the molten pool at both two ends during the DMD thin-walled part is worse, it is of great significance to analyze the thermal history of horizontal nodes [10,31]. As shown in Fig. 10, The temperature of the first peaks at the two endpoints (B_1 and B_5) is significantly higher than that at the middle points (B_2 , B_3 , and B_4). As the thermal conductivity of air is significantly lower than that of metal, a large amount of heat accumulates at the edges of the thin-walled part as the laser beam moves to the ends. Comparing the thermal cycle curves of other points, two temperature peaks with small-time intervals can be found on the thermal cycling curve at point B_1 at about 60s. The rapid change of direction as the laser head moves to the edge of the thin-walled part results in the appearance of small temperature peaks. As the heat builds up, these small temperature fluctuations are difficult to detect, as shown in Fig. 10. Besides, the number of temperature peaks at B_1 and B_5 is half of that at B_2 , B_3 , and B_4 , which indicates that the liquid metal at both ends of the thin-walled part has a longer cooling time.

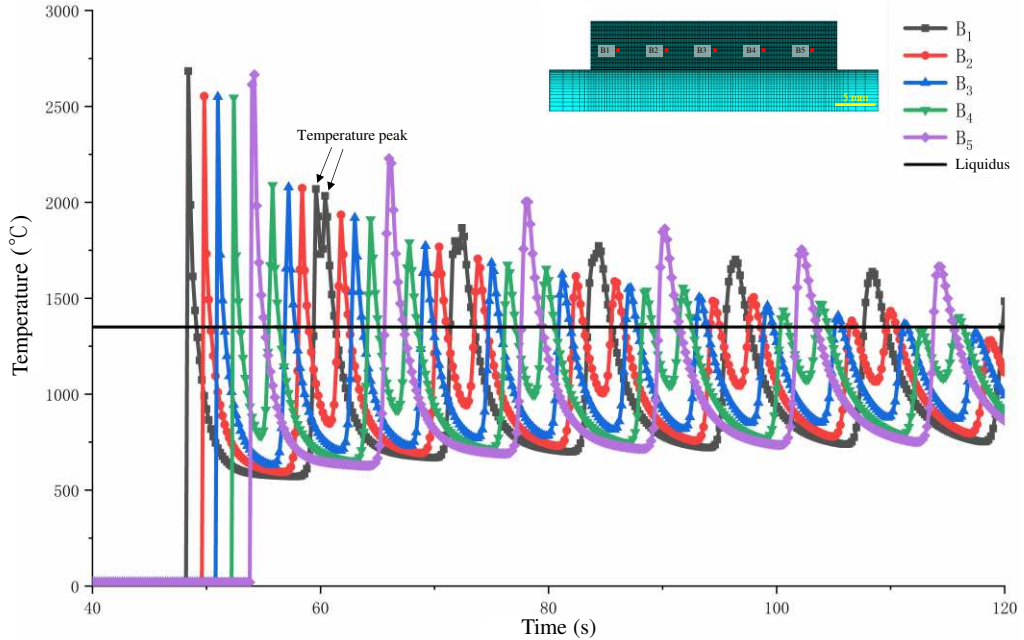


Fig. 10. Thermal cycle curves of different nodes on the 9th layer.

Fig. 11(a)–(c) shows the 2D temperature distribution of thin-walled parts at points B_1 , B_3 , and B_5 (see Fig.10). As shown in Fig. 11(a) and (c), the temperature distribution at the left side and the right side is not strictly consistent. Besides, the material at points B_1 and B_3 is heated by the laser twice in a relatively short time and then is heated again before the heat dissipation,

resulting in a large molten pool, which is consistent with the results in Fig. 10. This phenomenon might lead to the difference in the solidified microstructure between layers. The maximum temperature at locations along vertical lines passing through points B₁, B₃, and B₅ (see in Fig. 11(a)–(c)) of each deposition layer was extracted, the results are shown in Fig. 11(d). The temperature curve in the middle region of the thin-walled part presents a parabolic trend with the increase in the number of layers. While, the temperature at the two points on the edge of the thin-walled part tends to rise gradually in a sawtooth pattern. Besides, the difference between the maximum temperature and the lowest temperature is also increasing. This phenomenon is attributed to the poor heat dissipation conditions and long enough cooling time.

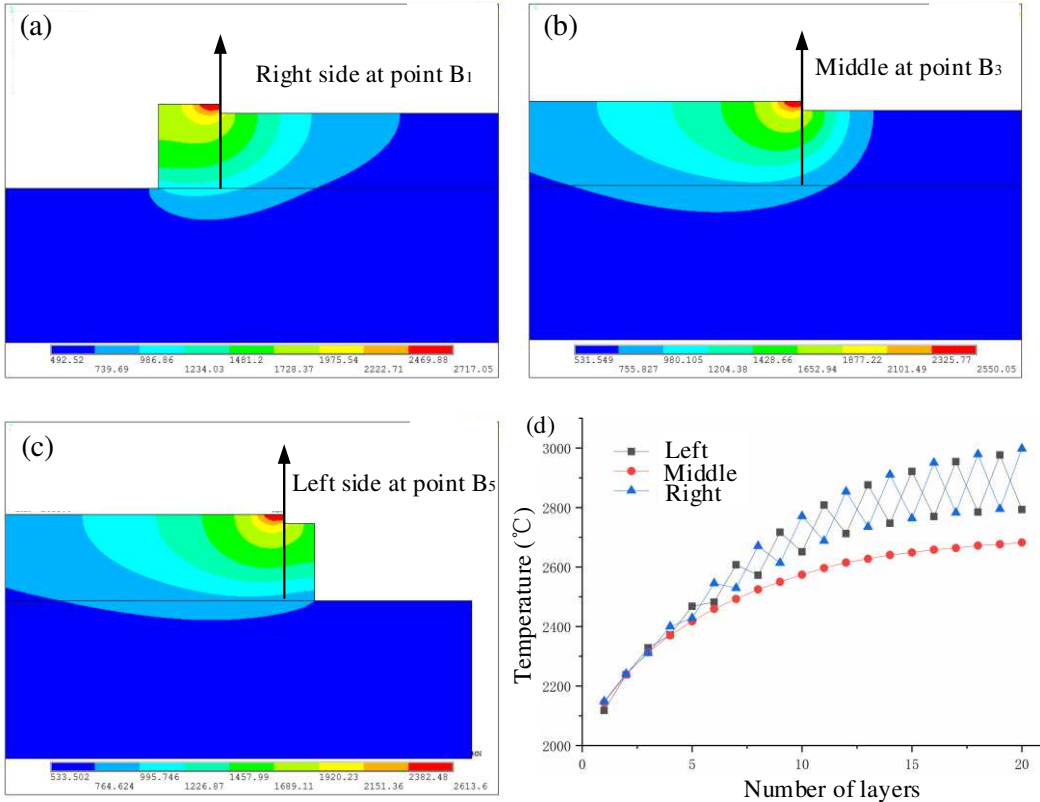


Fig. 11. (a)–(c), 2D Temperature distribution at the left side, middle, right side on the 9th layer; (d) the extracted temperature profiles at different locations along the building direction.

4.2 Optimized strategies

Gradually reducing the laser power and increasing the time interval between deposition layers can be considered as two effective methods to reduce the heat accumulation in the process

of DMD of thin-walled parts. When the necessary bonding ability between layers is considered, the limiting power P_{lim} required can be expressed as follows:

$$P_{lim} = \frac{Q_{lim}}{\eta} \quad (5)$$

where η is the utilization of laser energy, which can be obtained by a previous study [30], Q_{lim} is the limited energy required to remelting the former layer and can be defined by Eq. 6.

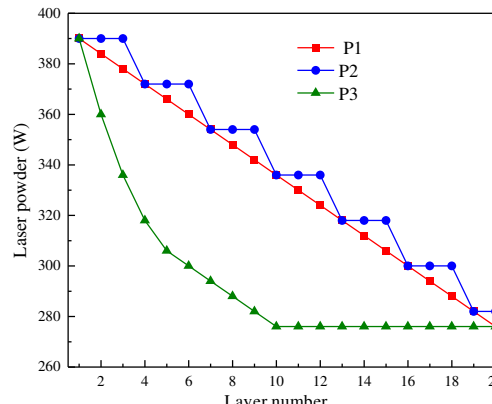
$$Q_{lim} = (S + \mu S) V_s \cdot \rho \cdot C_p^* (T_m - T_0) + \frac{kA(T_m - T_0)}{\sqrt{\pi\alpha t}} \quad (6)$$

where S is the cross-sectional area of a single track, μ is the ratio of the remelted zone and can be obtained by experimental, T_m is the liquids, T_0 is melting point, k is thermal conductivity, A is laser absorption coefficient, C_p^* is equivalent specific heat capacity, which can be defined by Eq. 7.

$$C_p^* = \frac{\Delta H}{T_m - T_0} + C_p \quad (7)$$

where ΔH is the enthalpy change due to solid-liquid transition, latent, C_p is specific heat capacity (Fig. 4). According to Eqs. 5–7, the limited power required for DMD of thin-walled parts is 280 W. Linear, step, and parabolic functions are used as the layer by layer decreasing mode of laser power. Optimized strategies carried out in this study are shown in Table 3.

Table 3 Optimized strategies for thin-walled parts during the DMD process.

Optimized object	Symbol	Optimization strategies
P1		
Laser powder	P2	
P3		
Time intervals	T5 T10 T15	5 s 10 s 15 s

Since the temperature field at the endpoint generated by the reciprocating scanning method is symmetrical, the computed results of the middle point and the left endpoint of each layer were selected to analyze the effect of the optimized strategies on the maximum temperature. As

shown in Fig. 12 (a) and (b), reducing laser power can improve the stability of the molten pool. When the 20th layer was built, the maximum temperature of the molten pool obtained by the three laser power optimization strategies (P1–3) is almost the same. The heat absorption and loss of the molten pool have reached a balance, and the heat accumulation of the former layer on the current layer can be ignored. The evolution of the maximum temperature under the strategies of P1 and P2 is almost the same. The temperature of the first 8 layers of the molten pool gradually rises. After that, with the continuous decrease of laser power, the heat absorbed by the former layer is equal to the heat dissipated. Fig.12(b) also shows that the temperature evolution at the endpoint is still serrated. From the above analysis, the temperature stability of the molten pool is best under the parabolic-shape power optimization, but the "sawtooth effect" still exists. Fig. 12(c) and (d) show the temperature evolution of the molten pool under the time intervals of 0s, 5s, 10s, and 15s. Although the maximum temperature was reduced by time interval optimization, its effect is less than that by the power adjustment. Besides, increasing the time interval would also reduce the deposition rate. This phenomenon shows that the gradual increase of the maximum temperature in the process of DMD thin-walled parts is mainly due to the transformation of the heat dissipation mechanism from three-dimensional to two-dimensional. The effect of the heat accumulation of the previous deposition on the current temperature field is secondary. Previous studies [12,13] have shown that the time intervals between layers is beneficial to release thermal stress. Compared with Fig. 12 (b) and (d), the "sawtooth effect" of temperature evolution at the left end of the deposition layer can be effectively alleviated by optimizing the time interval.

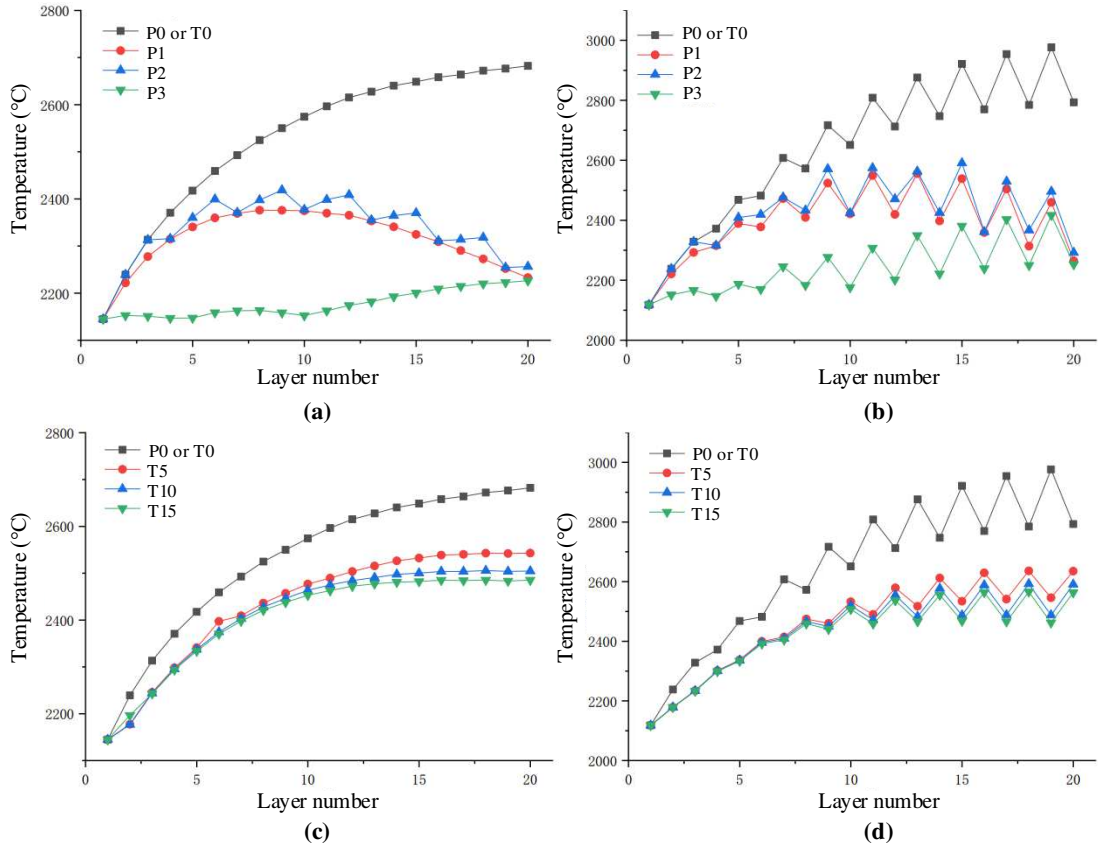


Fig. 12. Maximum temperature curves of the molten pool with increasing of the deposition layer after different optimized strategies. (a) and (c) Middle point; (b) and (d) Left point.

From the above analysis, the effect of decreasing the laser power gradually on the temperature stability of the molten pool is obvious. Its effect is not only superior to that of increasing the interlayer time interval but also does not reduce the deposition rate. Notably, it is not obvious to avoid the "sawtooth effect" in the process of deposition of thin-walled parts by optimized strategies of laser power (P1–P3). The time interval between layers can not only avoid the velocity fluctuation but also contribute to the heat loss. Therefore, the integrated optimized strategies of parabolic-like regulation (P3) and time interval (T5) were carried out, and the results are shown in Fig. 13. It can be seen that the temperature of about 2100 °C at the middle point and the endpoint of each layer is stable during the deposition process. In addition, the temperature fluctuation is significantly lower than that of a single optimized strategy. Therefore, the effect of an integrated optimized strategy (P3 & T3) on optimizing the maximum temperature of the molten pool is the most effective.

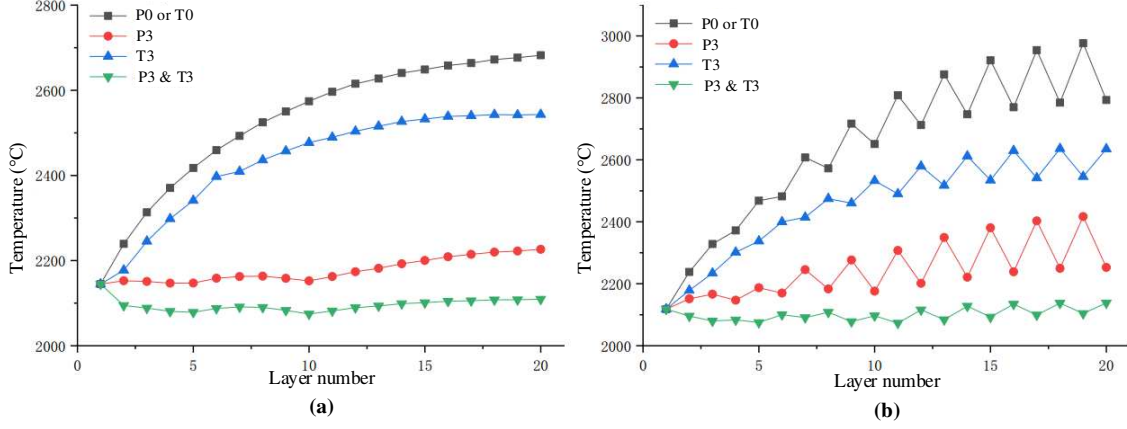


Fig. 13. Maximum temperature curves of the molten pool with increasing of the deposition layer under integrated optimized strategies. (a) Middle point; (b) Left point.

Fig. 14 shows the thermal cycle curves of the middle points in the first, fifth, tenth, fifteenth, and twentieth layers. The maximum temperature of the molten pool is almost coincident under the integrated optimization strategy. Four peaks are exceeding the liquids in the thermal cycle curves of all layers except the first layer, which indicates that the remelting times of each layer are two to three. The first layer only experienced two times of remelting because of the good heat dissipation of the substrate. The fifth deposited layer would undergo three remelting processes according to three temperature peaks. This phenomenon can achieve good bonding between layers. The same thermal cycle process is beneficial to improve the uniformity of microstructure and mechanical properties along the building direction.

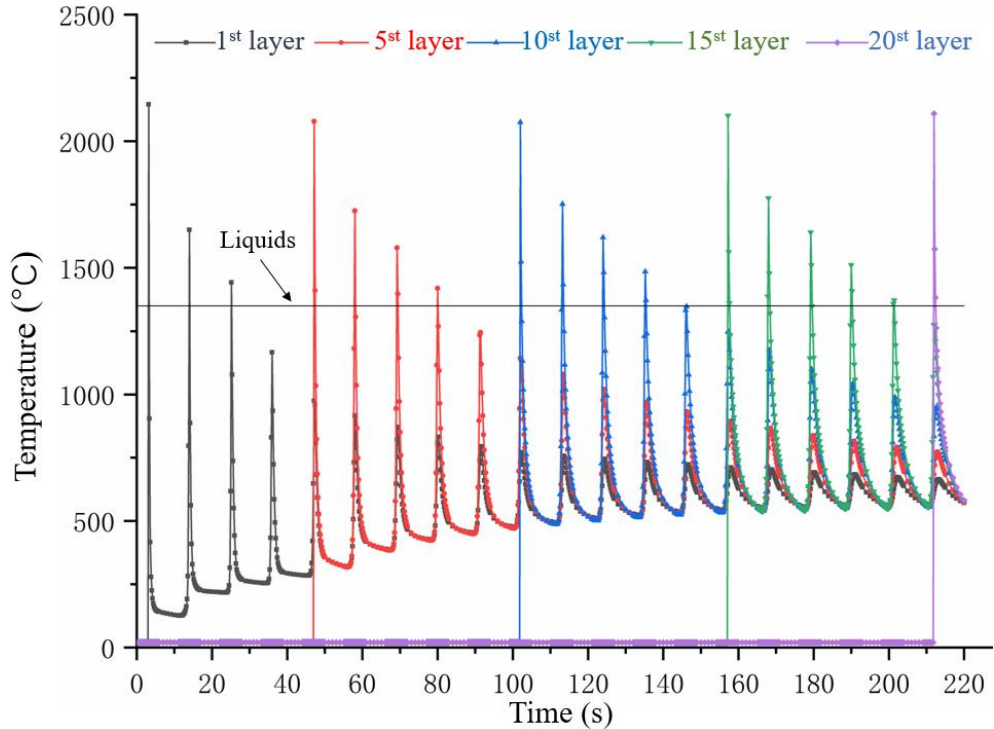


Fig. 14. Thermal cycle curves of deposition layer under integrated optimized strategies.

Due to the layer-by-layer accumulation, and rapid melting and solidification characteristics of the DMD process, the deposited materials would experience complex thermal history, which can lead to complex phase transformation and eventually form a variety of microstructures [5,32,33]. Fig. 15 represents the cooling rate of the middle points in the first, fifth, tenth, fifteenth, and twentieth layers under integrated optimized strategies. It can be seen that the changing trend of the cooling rate curve of each layer is almost the same, which gradually decreases and then tends to be stable with the increase of deposition layer. According to Fig.15, the solidified microstructure of the middle part of the thin-walled part can be inferred to be similar, while the microstructure at the bottom and top of the part is slightly different due to a bigger cooling rate and lack of subsequent heat treatment.

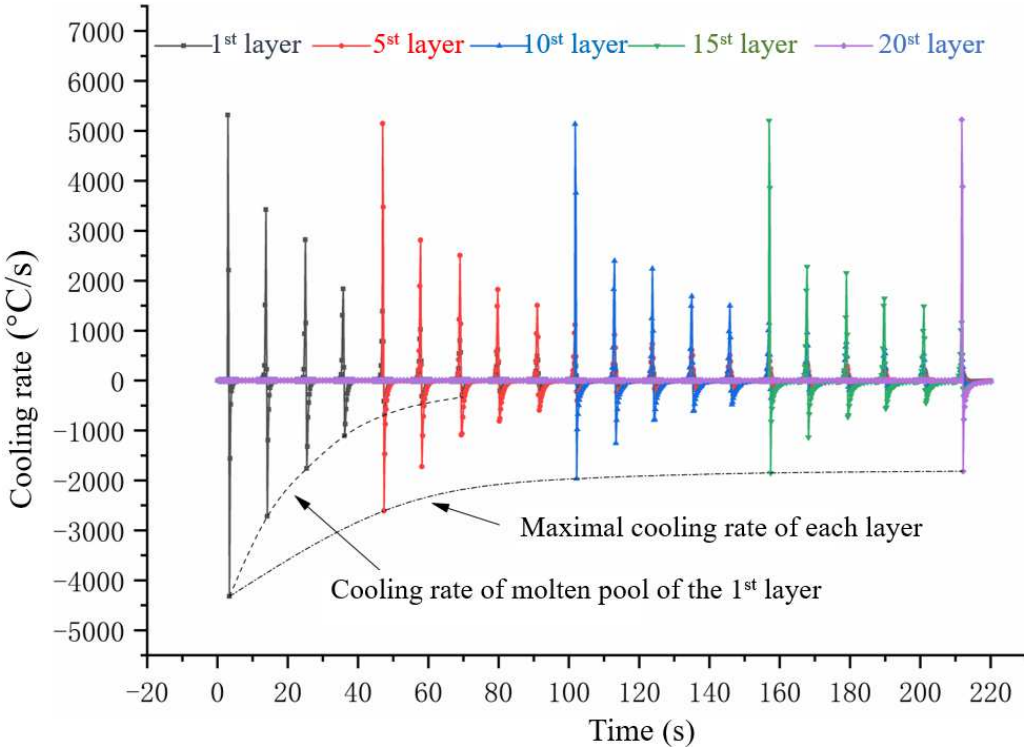


Fig. 15. The cooling rate of deposition layer under integrated optimized strategies.

4.3 Experiment verification

4.3.1 Cross-section morphology

The macro section morphologies of the thin-walled parts before and after optimization are shown in Fig. 16. It can be found that the width of the thin-walled parts with the integrated optimized strategy is more uniform, and its height is slightly higher than that of the thin-walled parts without optimization. Fig. 16 also shows that the width of the unoptimized thin-walled

part increases with the deposition height. Besides, the width error band at the bottom and top of Part 1 is wider than that at the middle. At the beginning of the deposition, the maximum temperature of the first layer is the lowest due to the good heat dissipation of the substrate (Fig. 9). Therefore, a smaller molten pool size would reduce the powder catchment efficiency [34], resulting in a smaller width of thin-walled parts. With the deposition process, the accumulation of heat promotes the increase of the size of the molten pool, which increases powder catchment efficiency, resulting in the bigger width of the solidified part. As shown in Fig. 14, the temperature of the molten pool of the thin-walled parts under an integrated optimized strategy is more stable. This behavior indirectly proves that the size of the molten pool almost does not change with the deposition height, so the mass of powder entering the molten pool is almost the same during the DMD process. Therefore, the width uniformity of the optimized thin-walled parts is better than that of the unoptimized one.

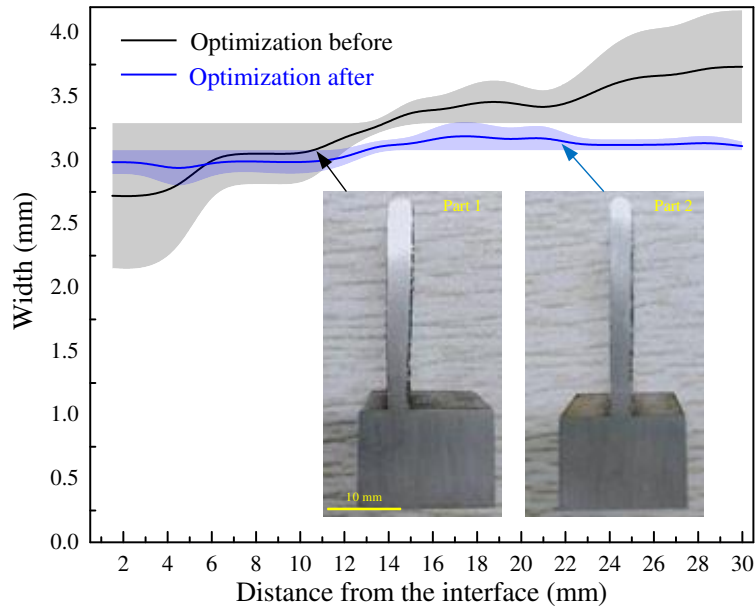


Fig. 16. Cross-section morphologies of thin-walled parts after the 20-layers build-process.
(a) Part 1 optimization before, (b) Part 2 optimization after.

4.3.2 Microstructure

Fig. 17 shows the typical microstructure of thin-walled parts at different positions before and after optimization. The micromorphology of solidified thin-walled parts has the characteristics of typical rapid solidification microstructure, mainly including dendrite, columnar, and equiaxed grains. As shown in Fig. 17(a)–(c), the microstructure at the bottom of the thin-walled parts without optimization is mainly composed of dendrites and columnar grains. These directional grains are mainly contributed to the large temperature gradient (G), which

easily leads to the anisotropy of mechanical properties of the parts, and then reduces the service life of the parts [35]. The microstructure in the middle of the part changes from directional dendrites to isotropic columnar and equiaxed grains. The accumulation of heat reduces the G in the molten pool, and the direction of heat conduction also changes from interlayer to both sides of the thin-walled part. With the increase of deposition height, the main part of heat loss is dominated by heat exchange and convection with the atmosphere, which leads to the increase of the number of equiaxed crystals. This phenomenon is similar to the study of Sun et al. [36]. As shown in Fig. 17(d)–(f), the microstructure at the bottom of the thin-walled parts with optimization is mainly composed of columnar, and equiaxed grains. The anisotropy of the microstructure of these optimized parts is weaker than that of the parts without optimization. As analyzed above, the temperature field of the molten pool becomes stable and the cooling rate decreases gradually. These are beneficial to reduce the G and lead to the generation of a large number of expected equiaxed grains.

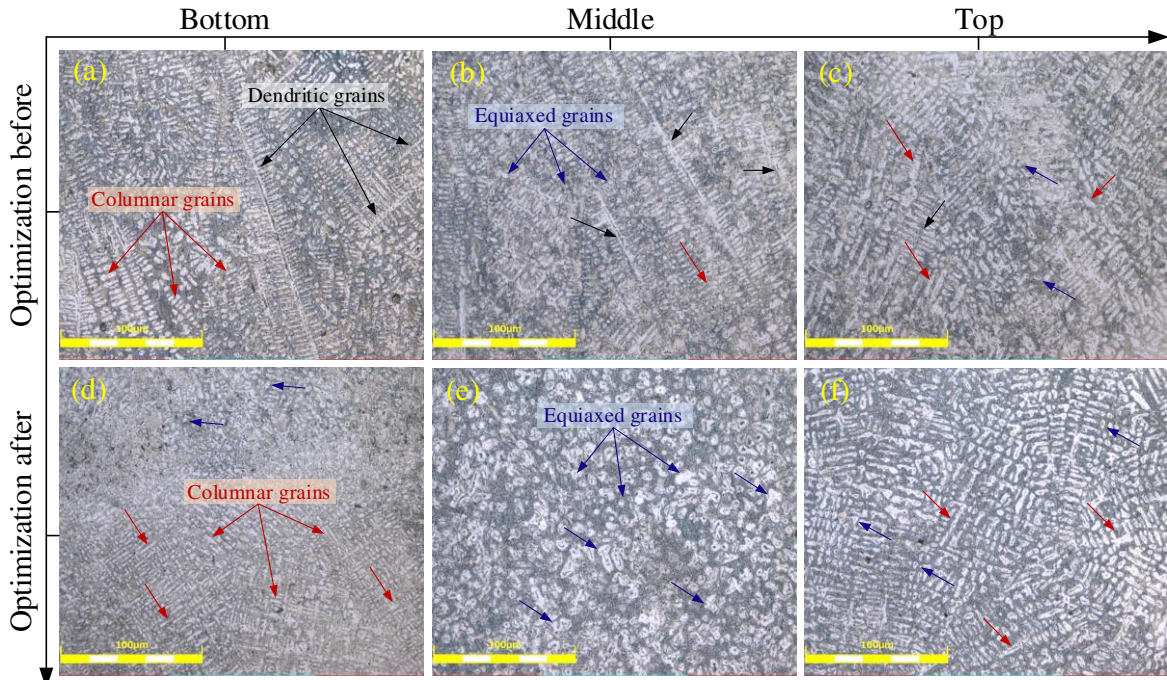


Fig. 17. The typical optical microstructure of (a)–(c) optimization before; (d)–(f) optimization after.

4.3.3 Microhardness distribution

The microhardness distribution along the building direction of optimized and unoptimized thin-walled parts is depicted in Fig. 18, which can be divided into four regions: substrate region I, bottom region II, middle region III, and top region IV. The microhardness of the thin-walled parts is larger than that of the substrate. This phenomenon shows that solidified phases of alloy

elements in metal powder are beneficial to increase the microhardness of the parts. In region I, the microhardness increases gradually along the building direction. The microhardness of the bonding zone between the thin-walled parts and the substrate increases sharply, which is mainly contributed to the strong convection in the molten pool [20]. This behavior leads to the full mixing of the elements in the alloy powder and the substrate, so the solidified hard phases can increase the microhardness of region I, significantly. In region II, the heat dissipation of the thin-walled part changes from three-dimensional to two-dimensional, and the heat dissipation becomes worse. Therefore, the microhardness in this region decreases slightly due to the repeated remelting and tempering heat treatment between the deposited layers. In region III, the fluctuation of microhardness of thin-walled parts is the smallest, which is due to the heat dissipation mechanism and the consistent thermal cycle of the deposition layer. In Region IV, the microhardness of thin-walled parts increases slightly. This is due to the absence of tempering heat treatment and the formation of a large number of equiaxed grains in this region. In addition, the evolution trend of microhardness with or without temperature optimization is almost the same. However, the average microhardness of thin-walled parts under integrated optimized strategies is higher than that without optimization, and the uniformity of microhardness distribution is better.

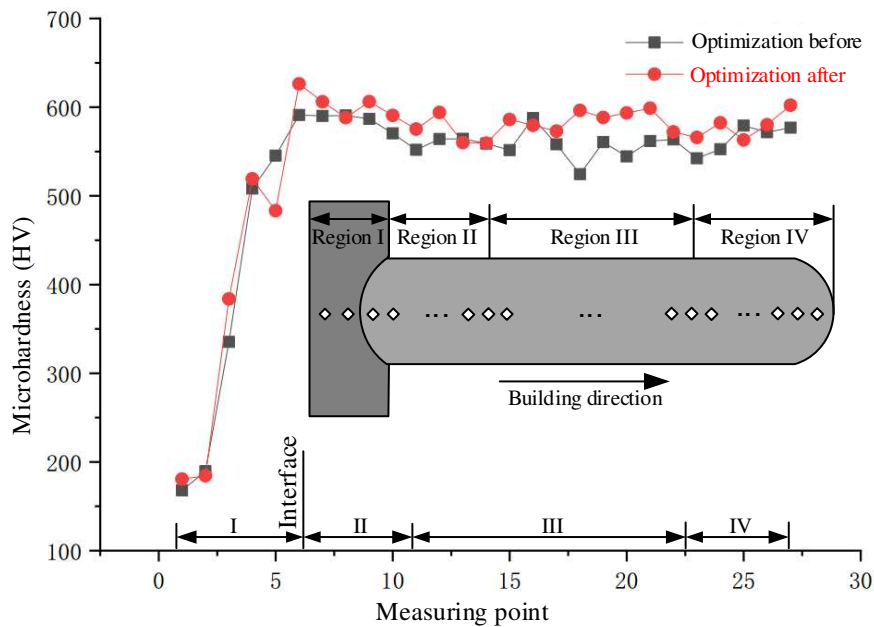


Fig. 18. The microhardness of optimized and unoptimized thin-walled parts along the building direction.

5. Conclusions

In this paper, an improved finite element model was first established to simulate the three-

dimensional heat dissipation process of thin-walled wall parts by the DMD process. Secondly, the temperature evolution of the molten pool was optimized by reducing the laser power and increasing the time interval. And then, the temperature cycle and cooling rate of thin-walled parts under the optimized strategy were analyzed. Finally, the cross-section morphology, microstructure, and microhardness of thin-walled parts are discussed in detail to verify the effect of the integrated optimized strategies on temperature evolution, geometric dimension, microstructure, and microhardness. The conclusions are as follows:

- (1) The optimization strategies of decreasing laser power and increasing time intervals can reduce the heat accumulation of the middle and endpoint points of thin-walled parts. The optimized strategy of gradually reducing the laser power is more significant than that of increasing time intervals.
- (2) During the DMD thin-walled parts, the heat accumulation is contributed to the transformation of heat dissipation from three-dimensional to two-dimensional, and the effect of the residual heat of the former layer on the heat accumulation of the current deposited layer is not significant.
- (3) The most significant effect is to reduce the heat accumulation in the DMD of thin-walled parts by adopting an integrated optimized strategy of gradually decreasing the laser power of the parabola shape and the time interval of 5s.
- (4) The thin-walled parts with an integrated optimized strategy have a more uniform cross-section size, finer microstructure, and higher microhardness.

Author contribution

Tianbiao Yu: Methodology, Modeling, Writing and editing, Experiment instruction, Supervision. **Liaoyuan Chen:** Writing-Original draft, Review, Investigation and experiment. **Zhe Liu:** Investigation and experiment, Simulation, **Pengfei Xu:** Experiment and Data curation.

Findings

This work was financially supported by the Fundamental Research Funds for the Central Universities (N2103004), and the National Natural Science Foundation of China (52075088).

Availability of data and materials

The data and materials that support the findings of this study can be shared upon request. All data generated or analyzed is presented within the study itself.

Declarations

Ethics approval Not applicable.

Consent to participate Not applicable.

Consent for publication Not applicable.

Conflict of interest The authors declare no competing interests.

References

1. Yan Z, Liu, W Tang, Z Liu, X Zhang, N Li, M and Zhang H (2018) Review on thermal analysis in laser-based additive manufacturing. *Opt Laser Technol* 106:427–441. <https://doi.org/10.1016/j.optlastec.2018.04.034>
2. DebRoy T, Wei HL, Zuback JS, Mukherjee T, Elmer JW, Milewski JO, Beese AM, Wilson-Heid A, De A, Zhang W (2018) Additive manufacturing of metallic components—Process, structure and properties. *Prog Mater Sci* 92:112–224. <https://doi.org/10.1016/j.pmatsci.2017.10.001>
3. Chen L, Yu T, Chen Y, Wang W (2022) Slicing strategy and process of laser direct metal deposition (DMD) of the inclined thin-walled part under open-loop control. *Rapid Prototyp J* 28:68–86. <https://doi.org/10.1108/RPJ-09-2020-0216>
4. Liu S, Hong KM, Katinas C, Shin YC (2019) Multiphysics modeling of phase transformation and microhardness evolution in laser direct deposited Ti6Al4V. *J Manuf Process* 45:579–587. <https://doi.org/10.1016/j.jmapro.2019.07.027>
5. Liu Z, Qi H (2015) Effects of substrate crystallographic orientations on crystal growth and microstructure formation in laser powder deposition of nickel-based superalloy. *Acta Mater* 87:248–258. <https://doi.org/10.1016/j.actamat.2014.12.046>
6. Ahsan MRU, Tanvir ANM, Ross T, Elsayy A, Oh M, Kim DB (2020) Fabrication of bimetallic additively manufactured structure (BAMS) of low carbon steel and 316L austenitic stainless steel with wire + arc additive manufacturing. *Rapid Prototyp J* 26:519–530. <https://doi.org/10.1108/RPJ-09-2018-0235>
7. Zhu G, Li D, Zhang A, Pi G, Tang Y (2012) The influence of laser and powder defocusing characteristics on the surface quality in laser direct metal deposition. *Opt Laser Technol* 44:349–356. <https://doi.org/10.1016/j.optlastec.2011.07.013>
8. Akbari M, Kovacevic R (2018) An investigation on mechanical and microstructural

- properties of 316LSi parts fabricated by a robotized laser/wire direct metal deposition system. *Addit Manuf* 23:487–497. <https://doi.org/10.1016/j.addma.2018.08.031>
- 9. Xiong J, Li R, Lei Y, Chen H (2018) Heat propagation of circular thin-walled parts fabricated in additive manufacturing using gas metal arc welding. *J Mater Process Technol* 251:12–19. <https://doi.org/10.1016/j.jmatprotoc.2017.08.007>
 - 10. Morville S, Carin M, Peyre P, Gharbi M, Carron D, Le Masson P, Fabbro R (2012) 2D longitudinal modeling of heat transfer and fluid flow during multilayered direct laser metal deposition process. *J Laser Appl* 24:032008. <https://doi.org/10.2351/1.4726445>
 - 11. Xia Z, Xu J, Shi J, Shi T, Sun C, Qiu D (2020) Microstructure evolution and mechanical properties of reduced activation steel manufactured through laser directed energy deposition. *Addit Manuf* 33:101114. <https://doi.org/10.1016/j.addma.2020.101114>
 - 12. Lu X, Lin X, Chiumenti M, Cervera M, Hu Y, Ji X, Ma L, Huang W (2019) In situ measurements and thermo-mechanical simulation of Ti–6Al–4V laser solid forming processes. *Int J Mech Sci* 153–154:119–130. <https://doi.org/10.1016/j.ijmecsci.2019.01.043>
 - 13. Biegler M, Graf B, Rethmeier M (2018) In-situ distortions in LMD additive manufacturing walls can be measured with digital image correlation and predicted using numerical simulations. *Addit Manuf* 20:101–110. <https://doi.org/10.1016/j.addma.2017.12.007>
 - 14. Akbari M, Kovacevic R (2019) Closed loop control of melt pool width in robotized laser powder-directed energy deposition process. *Int J Adv Manuf Technol* 104:2887–2898. <https://doi.org/10.1007/s00170-019-04195-y>
 - 15. Chunping H, Xin L, Fencheng L, Jun C, Fenggang L, Weidong H (2016) Effects of cooling condition on microstructure and mechanical properties in laser rapid forming of 34CrNiMo6 thin-wall component. *Int J Adv Manuf Technol* 82:1269–1279. <https://doi.org/10.1007/s00170-015-7453-z>
 - 16. Zhan MJ, Sun GF, Wang ZD, Shen XT, Yan Y, Ni ZH (2019) Numerical and experimental investigation on laser metal deposition as repair technology for 316L stainless steel. *Opt Laser Technol* 118:84–92. <https://doi.org/10.1016/j.optlastec.2019.05.011>
 - 17. Jiang Y, Cheng Y, Zhang X, Yang J, Yang X, Cheng Z (2020) Simulation and experimental investigations on the effect of Marangoni convection on thermal field during laser cladding process. *Optik (Stuttg)* 203:164044. <https://doi.org/10.1016/j.ijleo.2019.164044>

18. Zhang Q, Xu P, Zha G, Ouyang Z, He D (2021) Numerical simulations of temperature and stress field of Fe-Mn-Si-Cr-Ni shape memory alloy coating synthesized by laser cladding. *Optik* (Stuttg) 242:167079. <https://doi.org/10.1016/j.ijleo.2021.167079>
19. Javid Y, Ghoreishi M (2017) Thermo-mechanical analysis in pulsed laser cladding of WC powder on Inconel 718. *Int J Adv Manuf Technol* 92:69–79. <https://doi.org/10.1007/s00170-017-0117-4>
20. Chen L, Yu T, Xu P, Zhang B (2021) In-situ NbC reinforced Fe-based coating by laser cladding: Simulation and experiment. *Surf Coatings Technol* 412:127027. <https://doi.org/10.1016/j.surfcoat.2021.127027>
21. Song B, Yu T, Jiang X, Xi W, Lin X (2020) The relationship between convection mechanism and solidification structure of the iron-based molten pool in metal laser direct deposition. *Int J Mech Sci* 165:. <https://doi.org/10.1016/j.ijmecsci.2019.105207>
22. Chen L, Zhao Y, Song B, et al (2021) Modeling and simulation of 3D geometry prediction and dynamic solidification behavior of Fe-based coatings by laser cladding. *Opt Laser Technol* 139:107009. <https://doi.org/10.1016/j.optlastec.2021.107009>
23. Chen L, Zhao Y, Song B, Yu T, Liu Z (2022) Development of the molten pool and solidification characterization in single bead multilayer direct energy deposition. *Addit Manuf* 49:102479. <https://doi.org/10.1016/j.addma.2021.102479>
24. Bahrami A, Valentine DT, Helenbrook BT, Aidun DK (2015) Study of mass transport in autogenous GTA welding of dissimilar metals. *Int J Heat Mass Transf* 85:41–53. <https://doi.org/10.1016/j.ijheatmasstransfer.2015.01.074>
25. Zhang K, Wang S, Liu W, Shang X (2014) Characterization of stainless steel parts by Laser Metal Deposition Shaping. *Mater Des* 55:104–119. <https://doi.org/10.1016/j.matdes.2013.09.006>
26. Yu T, Sun J, Qu W, Zhao Y, Yang L (2019) Numerical and experimental investigation on laser metal deposition as repair technology for 316L stainless steel. *Opt Laser Technol* 118:84–92. <https://doi.org/10.1016/j.optlastec.2019.05.011>
27. Pang X, Zhou F (2020) Thermostability and weatherability of TiN/TiC-Ni/Mo solar absorption coating by spray method-laser cladding hybrid deposition. *Opt Lasers Eng* 127:. <https://doi.org/10.1016/j.optlaseng.2019.105983>
28. Tran HS, Tchuindjang JT, Paydas H, Mertens A (2017) 3D thermal finite element analysis

- of laser cladding processed Ti-6Al-4V part with microstructural correlations. *Mater Des* 128:130–142. <https://doi.org/10.1016/j.matdes.2017.04.092>
29. Wirth F, Wegener K (2018) A physical modeling and predictive simulation of the laser cladding process. *Addit Manuf* 22:307–319. <https://doi.org/10.1016/j.addma.2018.05.017>
30. Gan Z, Yu G, He X, Li S (2017) Numerical simulation of thermal behavior and multicomponent mass transfer in direct laser deposition of Co-base alloy on steel. *Int J Heat Mass Transf* 104:28–38. <https://doi.org/10.1016/j.ijheatmasstransfer.2016.08.049>
31. Wang S, Zhu L, Fuh JYH, Zhang H, Yan W (2020) Multi-physics modeling and Gaussian process regression analysis of cladding track geometry for direct energy deposition. *Opt Lasers Eng* 127:105950. <https://doi.org/10.1016/j.optlaseng.2019.105950>
32. Shamsaei N, Yadollahi A, Bian L, Thompson SM (2015) An overview of Direct Laser Deposition for additive manufacturing; Part II: Mechanical behavior, process parameter optimization and control. *Addit Manuf* 8:12–35. <https://doi.org/10.1016/j.addma.2015.07.002>
33. Gäumann M, Trivedi R, Kurz W (1997) Nucleation ahead of the advancing interface in directional solidification. *Mater Sci Eng A* 226–228:763–769. [https://doi.org/10.1016/s0921-5093\(97\)80081-0](https://doi.org/10.1016/s0921-5093(97)80081-0)
34. Tan H, Shang W, Zhang F, Clare AT, Lin X, Chen J (2018) Process mechanisms based on powder flow spatial distribution in direct metal deposition. *J Mater Process Technol* 254:361–372. <https://doi.org/10.1016/j.jmatprotec.2017.11.026>
35. Bermingham MJ, StJohn DH, Krynen J, Tedman-Jones S (2019) Promoting the columnar to equiaxed transition and grain refinement of titanium alloys during additive manufacturing. *Acta Mater* 168:261–274. <https://doi.org/10.1016/j.actamat.2019.02.020>
36. Sun J, Zhao Y, Yang L, Zhao X, Qu W, Yu T (2019) Effect of shielding gas flow rate on cladding quality of direct laser fabrication AISI 316L stainless steel. *J Manuf Process* 48:51–65. <https://doi.org/10.1016/j.jmapro.2019.10.011>

Supplementary Files

This is a list of supplementary files associated with this preprint. Click to download.

- [DeclarationofCompetingInterest.docx](#)